ON THE FLOW STRUCTURES UNDER A PARTIALLY INUNDATED BRIDGE DECK

C. Lin * **M.-J. Kao** **S.-C. Hsieh** **L.-F. Lo**

Department of Civil Engineering
National Chung Hsing University
Taichung, Taiwan 40227, R.O.C.

R. V. Raikar

Department of Civil Engineering
K. L. E. S. College of Engineering and Technology
Belgaum 590008, India

ABSTRACT

This paper presents the flow structure under a partially inundated bridge deck measured by using particle image velocimetry (PIV) and flow visualization techniques. The approaching flow was subcritical having Froude number F in the range 0.12 ~ 0.55. The proximity ratio P_r (= ratio of clearance below the bridge deck h to the total depth of deck D) was varied from 0.57 to 2. Depending upon the Froude number F and proximity ratio P_r, four types of flow structures under the bridge deck were recognized. In flow Type I, the water surface elevation on the downstream side of bridge deck is slightly lower than the counterpart on the upstream side, and the shear layer formed at the bottom of upstream girder continuously fluctuates and touches soffit of all girders. In the case of flow Type II, the water surface on downstream side of bridge deck is lower than that on the upstream side and the shear layer originating from the upstream girder impinges near the third cavity between girders. However, in both the cases, the cavities between the girders are completely occupied by vortices. On the contrary, in the cases of flow Type III and flow Type IV, the flow is separated from the upstream girder edge. However, in flow Type III, the separated flow impinges on successive girders and cavities are partially filled by water; while in flow Type IV, the flow is totally separated from the deck bottom like orifice flow. The phenomena of vortex formation within the cavities are discussed for the cases of flow Type I and flow Type II. Also, for the vertical distribution of mean streamwise velocity in the shear layer below bridge deck, the nonlinear regression equations are developed. Using the distributions of measured mean streamwise velocity within the shear layer below the bridge deck at different streamwise distances, the similarity profile is obtained. The mean velocity deficit ($u_{sl} - u_{su}$) and representative thickness b_s are considered as the appropriate characteristic velocity and length scales for developing similarity profile. The proposed characteristic scales provided unique similarity profiles having promising regression coefficient. The similarity profile proposed is suitable for more general case of bridge deck having different bridge girders and even for rectangular block without girder. Further, the turbulence characteristics for the flow below the bridge deck are also presented.

Keywords: Bridges, Pressured flow, Inundated flow, Flow visualization, Particle image velocimetry, Shear layer, Similarity profile, Turbulence.

1. INTRODUCTION

Bridges form the vital joints in the road as well as railway network systems constructed at river crossings. Their evaluation during the design and construction as well as during and after flooding plays a critical role for the hydraulic or bridge engineers. Failures of many bridges due to scour at bridge piers and abutments is a common phenomenon. Even though numerous investigations including laboratory and field studies including laboratory and field studies focused on various phenomena of bridge failures [1-5], they mainly focused on free surface flow and scour depth. During peak floods, the water level in the rivers continuously rises. The bridges in the upstream reach experience the gradual increase in water level and get submerged either partially or totally. On the other hand, the bridges at the lower reaches are subjected to unexpected flood and consequently get inundated.

* Corresponding author (chenglin@nchu.edu.tw)

DOI : 10.1017/jmech.2012.20
Copyright © 2012 The Society of Theoretical and Applied Mechanics, R.O.C.
https://doi.org/10.1017/jmech.2012.20 Published online by Cambridge University Press

Such submerged bridges are subjected to the significant back water effect and large amount of hydrodynamic forces. In addition, the debris flow that include large amount of boulders and floating wooden logs induces the additional impact on the bridge decks. Such inundated bridges will be subjected to a combined effect of pressure flow below the bridge deck and the weir flow over the bridge depending upon the water level of the approaching flow relative to the headroom clearance below the bridge deck. The pressure flow also known as orifice flow [5] or vertical contraction flow occurs when the water level on the upstream side of deck is above the bottom surface of the partially submerged girder. On the other hand, when the water level rises above the bridge deck, along with the pressure flow the weir flow occurs and overtops the bridge deck. Figure 1(a) shows the picture of Da-Chie Bridge partially inundated by the flood which was triggered by typhoon Nari on September 17, 2001; and Fig. 1(b) also demonstrates the photo of Cyuan Zih She Bridge overtopped by the flood during typhoon Morakot on August 8, 2010 in Taiwan. The flow instability and vortex formation create the wave motion between the bridge girders [6] and maximum peak hydrodynamic load acting on the bridge can cause the displacement of bridge deck. In addition, with an enhanced effect of pressurized flow along with three dimensional flow structures around bridge piers, the maximum scour depth at bridge piers might become 2.3 to 10 times the scour depth due to free surface flow conditions [7]. Consequently, the bridges subjected to inundated conditions are more liable to failure.

In this context, previous studies of such inundated bridges can be grouped under two classes: Hydrodynamic loading on the bridge deck along with the effect of various parameters and scour below the inundated bridge deck. Naudascher and Medlarz [6] determined the force coefficients theoretically as well as experimentally to express the hydrodynamic forces acting on the submerged bridge deck and the associated loss in channel flow. They used momentum and energy equations to compute the force coefficients. The force coefficients suggested by Naudascher and Medlarz [6] can be used to estimate the peak hydrodynamic loading acting on the bridge deck induced by flow instability and vortex formation. Jempson [8] measured hydrodynamic and debris loadings on the laboratory scaled model of submerged bridge deck and piers. The results were expressed in terms of drag, lift and moment coefficients which were dependent on Froude number, degree of submergence and proximity ratio. He also studied the effects of these parameters on the force and moments along with turbulence intensity, super elevation and skew. In addition, Jempson [8] presented the flow patterns around the bridge decks such as boundary layer separation and reattachment, free surface effects and wake blockage effects. The equations for the discharge and back water calculation behind partially and fully submerged rectangular bridge deck were presented by Picek *et al*. [9]. For fully submerged bridge deck, Picek *et al*. [9] used energy-balance method for prediction of total discharge without dividing it into pressure flow and weir flow components.



(a)



(b)

Fig. 1 (a) Picture of Da-Chie Bridge partially inundated by the flood which was triggered by typhoon Nari on September 17, 2001; (b) Photo of Cyuan Zih She Bridge overtopped by the flood during typhoon Morakot on August 8, 2010 in Taiwan. [Fig. 1(b) is the courtesy of the Fifth Maintainance Office, Directorate General of Highways, MOTC.]

On the other hand, the pioneering work on the pressure-flow scour was conducted by Abed [10] at Colorado State University. She conducted free surface flow and pressure-flow pier scour experiments. However, Abed [10] did not separate the two scour components. Umbrell *et al*. [7] developed an empirical equation for the prediction of pressure-flow contraction scour depth at bridge piers using experimental results. They suggested that, this pressure-flow contraction scour depth when added with local scour at piers or abutments computed by HEC-18 will result in total scour depth at submerged piers. Later, Arneson and Abt [11] derived a multiple regression equation for the vertical contraction scour below the bridge deck and same was recommended by HEC-18 [5]. Also HEC- 18 mentioned that pier scour could be increased by 200 to 300% by pressure flow. Verma *et al*. [12] investigated the effect of constriction due to bridge submergence on the scour depth considering the effect of various factors such as velocity and depth of approaching flow, degree of submergence and width of bridge. They found that at incipient condition the maximum scour depth was equal to the constricted flow width. A factor of 1.5 was suggested by Verma *et al*. [12] for predicting the maximum scour depth under submerged bridge.

https://doi.org/10.1017/jmech.2012.20 Published online by Cambridge University Press

Later, Lyn [13] reexamined HEC-18 equation and proposed an alternate equation for the prediction of scour depth under pressure-flow. The new equation combined power-law relationship with an asymptotic constant value. The proposed design equation was based on one-sided prediction interval. Recently, Junke *et al*. [14] classified the scour at the bridge into three types, namely, downstream unsubmerged, partially submerged and totally submerged case. They proposed the equations for the determination of maximum scour depth for bridge pressure flow at different flow conditions. Junke *et al.* [14] also developed similarity profile for the bed profiles and the design procedure for the field evaluation of scour depth.

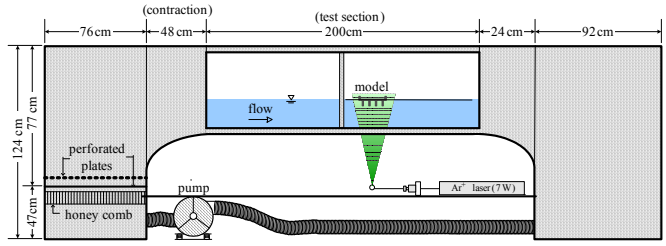
All the above mentioned studies emphasized mainly either on computation of hydrodynamic forces or on the prediction of scour depth below the bridge. However, no studies were reported on the investigations of the flow structure below the inundated bridge piers either partially or fully, except Malavasi and Blois [15] who studied the influence of free surface on the flow patterns around a rectangular cylinder. They used PIV to measure the mean flow structure and related the cylinder submergence with the dimension and position of vortex structure along with hydrodynamic loading on the cylinder. Nevertheless, their study was limited to flow around rectangular bluff body. Therefore, the present paper focuses mainly on the measurement of velocity characteristics of flow structure below the partially inundated bridge deck. Flow visualization and PIV techniques were used to measure the flow field. The flow structure below the bridge deck is divided into four types depending upon parameters of approaching flow and dimensions of bridge deck. For the shear layer stemming from the bottom of upstream girder below the bridge deck, the similarity profile is obtained for the mean streamwise velocity considering the flow Type I and flow Type II. Further, the turbulence characteristics within the flow below the bridge deck are also illustrated. It is pertinent to mention that in this study the authors have concentrated only on the flow structure below the partially inundated bridge deck. However, experimental study for the flow characteristics under fully inundated bridge deck is in progress. Further, this study only focuses on the flow phenomenon without considering the scour of mobile beds. The authors believe that the data provided in this study facilitate the researchers in numerical modeling and also enhance the knowledge of flow phenomenon.

2. EXPERIMENTATION

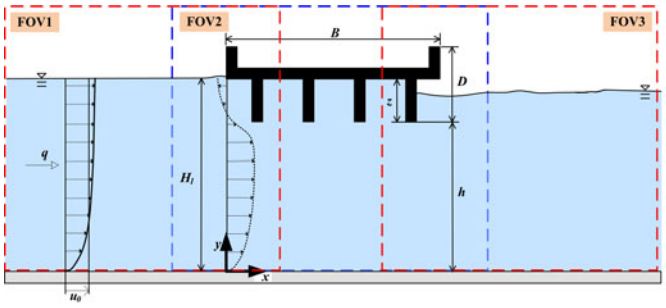
Experiments were carried out in a recirculating flume 446cm long and 25cm wide, located at the Hydraulics Laboratory of the Department of Civil Engineering, National Chung Hsing University, Taiwan. The test section was fitted with glass-sided walls and glass bottom to facilitate optical access and was located at 150cm from the inlet of the flume. The internal dimensions of the test section were 200cm long, 25cm wide and 52.5cm deep. The schematic view of the flume fitted with bridge deck model along with PIV arrangements is illustrated Fig. 2(a). The bridge deck model was made of acrylic sheet and was also 1:100 scaled down model simulated from the bridges on Taiwan provincial routes 20 and 21 in south part of Taiwan. The overall width B and total depth D of bridge deck model was 10.0cm and 3.5cm, respectively. It has four girders of 2.0cm depth and 0.5cm width spaced at 2.4cm center-to-center. The bridge deck model was fitted in the test section so that its position from the flume bottom can be adjusted depending upon the required proximity ratio P_r. The proximity ratios P_r considered in the present study were 0.57, 1.0, 1.42 and 2.0. In the approaching section of the flume, the stilling basin consisted of honeycomb structure, perforated steel plates and a contraction section which assisted in obtaining the smooth approaching flow. The flow was regulated through a control unit having a feedback circuit and a butterfly valve. The approaching flow was two-dimensional and uniform which was verified in detail by measurements of the mean streamwise velocity along the upstream direction (details available in Lo [16]). The approaching flow depth H_1 was so adjusted that for each case of proximity ratio P_r considered, the water surface was at the top level of the girders as seen from Fig. 2(b). Figure 2(b) also indicates the FOVs used for PIV measurements and the coordinate system considered in the present study. The origin of the coordinate system is located immediately below the upstream edge of the deck with x measured downstream along the flume bottom and y measuring normal to flume bottom upwards. In Fig. 2(b), q indicates the discharge per unit width ($= u_0 \times H_1$) and u_0 represents mean approaching flow velocity. The approaching flow Froude number F ($= q/\sqrt{gH_1^3}$, where g = gravitational acceleration) was ranging between 0.12 and 0.55 and Reynolds number R ($=\rho u_0 H_1/\mu$, where μ = dynamic viscosity) in the range of 4992 – 49257. The range of experimental conditions for all cases (or Cases/Series $A \sim O$) is given in Table 1. Also, the bridge decks consisting of three girders (Case P) and a rectangular block without girder (Case Q) were also used in the study in order to expand the study area and applicability.

For PIV measurements and flow visualization techniques, two major instruments used were the argon-ion laser (Coherent Innova-300) and high speed camera (Phantom V5.1 from Vision Research). In the PIV system, the 7W argon-ion laser was used as a light source for the measurement the two-dimensional velocity field below the inundated bridge deck. The laser beam emitted from the source was reflected by a series of mirrors and then passed through a glass cylinder of 0.57cm diameter to spread into a fan-shaped light sheet of 1.5mm thick as demonstrated in Fig. 2(a). Aluminum powder particles with a mean diameter of 10.0μm and specific gravity of 2.7 were used as seeding tracer in PIV. The settling velocity of aluminum particles estimated from Stokes' law was about 0.093cm/s, which was much smaller than the average flow velocity used in the present study.

https://doi.org/10.1017/jmech.2012.20 Published online by Cambridge University Press



(a)



(b)

Fig. 2 (a) Schematic diagram of flume along with bridge deck model and PIV system, (b) Schematic diagram illustrating FOVs, coordinate system and definition variables

Table 1 List of experimental conditions for all cases (or series)

Case / Series	Model Type	h (cm)	$P_r = h / D$	H_1 (cm)	u_0 (cm / s)	$q = u_0 \times H_1$ (cm^2 / s)	$F = \frac{q}{\sqrt{g \times H_1^3}}$	$R = \frac{\rho u_0 H_1}{\mu}$
A	4 girders	7.0	2.00	9.0	12.06	109	0.13	10854
B	4 girders	7.0	2.00	9.0	18.41	166	0.20	16569
C	4 girders	7.0	2.00	9.0	31.40	283	0.33	28260
D	4 girders	7.0	2.00	9.0	33.64	303	0.36	30276
E	4 girders	7.0	2.00	9.0	47.88	431	0.51	43092
F	4 girders	7.0	2.00	9.0	54.73	493	0.55	49257
G_{series}	4 girders	7.0	2.00	9.0	12.34 ~ 44.27	111 ~ 398	0.13 ~ 0.47	11106 ~ 39843
H_{series}	4 girders	7.0	2.00	9.0	15.75 ~ 48.20	142 ~ 434	0.17 ~ 0.51	14175 ~ 43380
I_{series}	4 girders	5.0	1.42	7.0	9.63 ~ 43.80	67 ~ 307	0.12 ~ 0.53	6741 ~ 30660
J_{series}	4 girders	5.0	1.42	7.0	15.84 ~ 41.46	111 ~ 290	0.19 ~ 0.50	11088 ~ 29022
K	4 girders	3.5	1.00	5.5	17.40	96	0.24	9570
L_{series}	4 girders	3.5	1.00	5.5	11.10 ~ 39.9	61 ~ 219	0.15 ~ 0.54	6105 ~ 21945
M_{series}	4 girders	3.5	1.00	5.5	18.10 ~ 37.33	100 ~ 205	0.25 ~ 0.51	9955 ~ 20532
N_{series}	4 girders	2.0	0.57	4.0	13.93 ~ 26.79	56 ~ 107	0.22 ~ 0.46	5572 ~ 10716
O_{series}	4 girders	2.0	0.57	4.0	12.48 ~ 28.19	50 ~ 113	0.20 ~ 0.45	4992 ~ 11276
P	3 girders	7.0	2.00	9.0	18.58	167	0.20	16722
Q	rectangle	7.0	2.00	9.0	19.12	172	0.20	17208

A high speed camera having a huge internal memory block (2GB), 1024 × 1024 pixel resolution, 10-bit dynamic range, and 1200Hz maximum framing rate was used to capture images of the particle laden flow. The large internal memory block permits 2027 frames at full resolution to be saved successively. The camera fitted with 60mm and 200mm focal lens was operated at 600 ~ 1,000 frames per second throughout the experiments. The captured images were processed using commercial software TSI Inc and the velocity fields were determined by cross-correlation analysis. A multi-grid process starting from 32 × 32 pixels and ending with 8 × 8 pixels for interrogation windows with 50% overlap were used in the cross-correlation analysis. The images from three fields of views (FOVs) of size 16.417cm × 16.417cm were taken using PIV [see Fig. 2(b)] with the corresponding length of a grid element in the velocity vector field is thus $\Delta x = \Delta y = 0.128$cm. On the other hand, near the bottom boundary layer, the field of view for the PIV camera was set to an area of 3.012cm × 1.506cm in the flow, the corresponding length of a grid element in the velocity vector field is thus $\Delta x = 0.047$cm and $\Delta y = 0.012$cm. In addition, the high speed camera resolution near the bottom boundary layer was 1024 × 512 pixels and cross-correlation analysis was done using a multi-grid process starting from 64 × 16 pixels and ending with 16 × 4 pixels for interrogation windows with 50% overlap. The use of high speed camera not only helped to capture the images at the rate of 600 ~ 1,000 frames per second, but also provided instantaneous maps of velocity field, aiming to achieve high spatial resolution as well as high temporal resolution. Further, the framing rate and total duration of PIV for each run are 600 ~ 1,000Hz and 32.0 ~ 86.7 sec, respectively.

In flow visualization technique, the particle path line photography was used for qualitative flow pattern observations. Aluminum powder particles used in PIV were also used as seeding tracers in the flow visualization experiments. The 7W argon-ion laser beam and the high speed camera were both employed as the light source and the image acquisition equipment, respectively, with the same setup in the PIV system described above.

3. RESULT AND DISCUSSIONS

3.1 Classification of Flow Type Under Bridge Deck

Four different cases of idealized flow patterns were identified below the bridge deck, depending on the approaching Froude number F, Reynolds number R and proximity ratio P_r. Figures 3(a) ~ 3(d) illustrates the schematic diagrams of four flow types along with the flow visualization pictures for the cases having proximity ratio $P_r = 2.00$. The salient features of four cases of flow types are given below:

Type I The shear layer formed at the bottom edge of the upstream girder continuously fluctuates and touches the soffit of all the girders. The

https://doi.org/10.1017/jmech.2012.20 Published online by Cambridge University Press

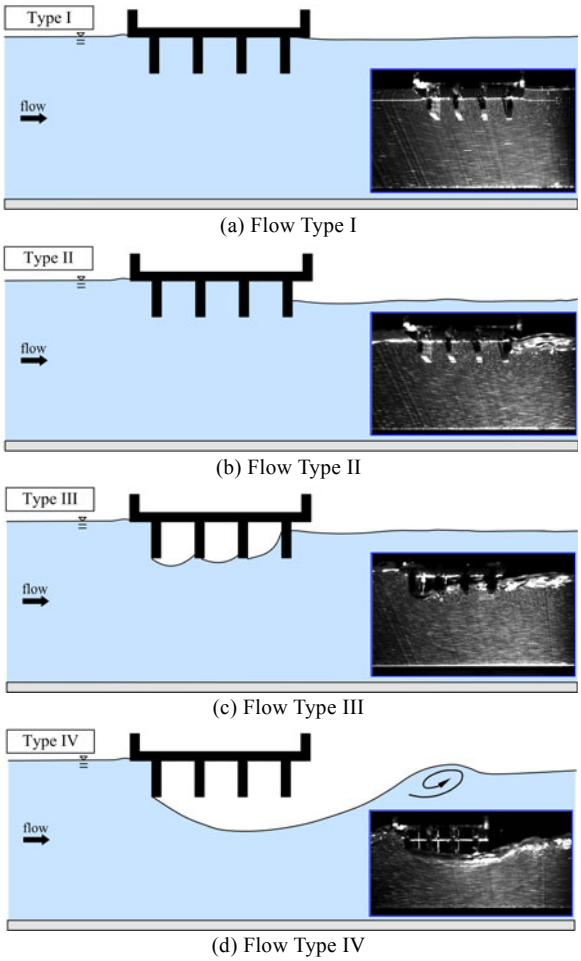
vortices are formed in all the three cavities between the girders. The vortices in the second and third cavities are stronger and distinct than the first cavity. It is because the shear layer originating from the upstream girder and thereafter striking the second girder creates the reverse flow that enters into the first cavity thereby reducing the size and strength of vortex. On the contrary, the vortices in the remaining two cavities are stronger and get fed by the shear layer continuously. Note that the water surface elevation on the downstream side of the bridge deck is slightly lower than the counterpart on the upstream side [Fig. 3(a)]. This type of flow is found to occur for smaller ranges of Froude number and Reynolds number [see Figs. 4(a) ~ 4(b)].

Type II In this case, the shear layer directly impinges near the third cavity of the bridge deck. A small vortex is formed in the first cavity very close to the shear layer but washed out frequently by the shear layer. On the other hand, the second and third cavities are filled with strong vortices. The water surface elevation on the downstream side of the bridge deck is lower than that on the upstream side [Fig. 3(b)].

Type III The shear layer is separated at the bottom edge of the upstream girder in the form of jet flow. This jet impinges on all the girders. However, all the three cavities are partially filled with water. Large fluctuations are observed in the water surface elevation on downstream side of the bridge deck [Fig. 3(c)].

Type IV The flow is separated completely from the bottom of the deck. It is similar to orifice flow below the bridge deck as indicated by Richardson and Davis [5] [Fig. 3(d)]. This type of flow is found to occur for higher ranges of Froude number and Reynolds number [see Figs. 4(a) ~ 4(b)].

Figures 4(a) ~ 4(b) illustrate the classification of four flow types depending upon proximity ratio P_r, Froude number F and Reynolds number R as indicated by demarcation lines. For $P_r = 2.00$, Type I flow is found to occur for $F < 0.28$ and $R < 23500$, flow Type II occurs in the range of $F = 0.28 \sim 0.44$ and $R = 23500 \sim 37350$, flow Type III occurs for $F = 0.44 \sim 0.495$ and $R = 36900 \sim 41900$, while Type IV flow occurs when $F > 0.495$ and $R > 41900$. However, these ranges narrow down as the proximity ratio P_r decreases. It is because with the decrease in P_r, the flow velocity below the bridge deck increases prominently and hence Froude number and Reynolds number also increase. The above classification can also be illustrated using the ratio H_1 / h in place of proximity ratio P_r as shown in Fig. 5. It is important to mention that the ratio H_1 / h in Fig. 5 is $H_1 / h = 1 + z / DP_r$. As depth of girders, z (refer Fig. 2) and total depth of deck D are constants; H_1 / h is inversely proportional to proximity ratio P_r.



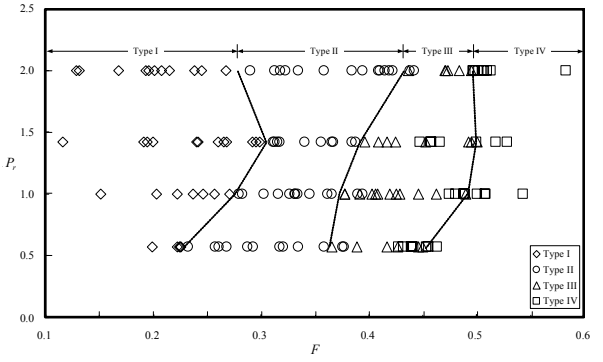
(a) Flow Type I

(b) Flow Type II

(c) Flow Type III

(d) Flow Type IV

Fig. 3 Schematic diagram of flow types below bridge deck for proximity ratio $P_r = 2.0$

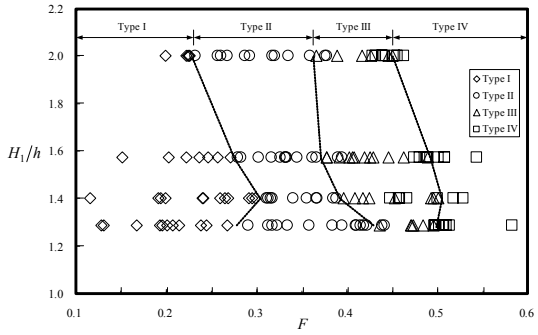


(a) Proximity ratio P_r and Froude number F

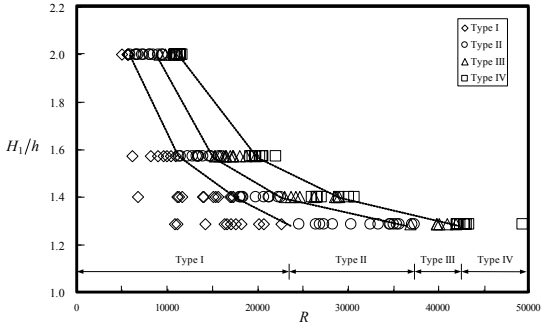
(b) Proximity ratio P_r and Reynolds number R

Fig. 4 Classification of flow types

https://doi.org/10.1017/jmech.2012.20 Published online by Cambridge University Press



(a) H_1/h and Froude number F



(b) H_1/h and Reynolds number R

Fig. 5 Classification of flow types

Further, it is important to mention that, the flow right beneath the bridge deck is subcritical for flow Type I to flow Type III, while it is supercritical for flow Type IV. To check the flow condition, the Froude number was calculated for flow Type IV. It was found that the Froude number calculated using Belanger equation [$y_2 / y_1 = 0.5(-1+\sqrt{1+8F_B^2})$, where F_B = Froude number calculated by Belanger equation] below the bridge deck at the location of minimum flow depth y_1 is 1.25, while that computed from velocity measurements obtained by PIV is 1.24. This confirmed the flow condition for Type IV as supercritical [16]. Also it is corroborated by the formation of hydraulic jump downstream of the bridge deck as visualized by Fig. 3(d). Note that for all cases Type I to Type IV the flows downstream of bridge deck are subcritical.

3.2 Flow Structure in the Cavities

In this section the flow structure within the cavities between the girders is demonstrated. However, only flow Type I and flow Type II cases are considered, because in the cases of flow Type III and flow Type IV the shear layer separates out from the bottom edge of the upstream girder and hence no vortex formation occurs in the cavities.

Type I:

In this case the approaching Froude number is very low (in the present study F = 0.20). As the flow passes below the bridge deck girders, a shear layer stems out from the bottom edge of the upstream girder. Very weak and ill-defined vortices are formed between the shear layer and the first cavity, which keep growing as a result of shear layer fluctuation. With the progress of time, the reverse flow from second cavity generates a secondary vortex of clockwise direction in the first cavity near the face of second girder [Fig. 6(a)]. This clockwise vortex becomes larger and stronger as depicted in Fig. 6(b). At the same time another vortex forms in between the second girder and shear layer which pushes the earlier clockwise vortex upwards into the first cavity [see Fig. 6(c)]. However, this vortex formed near the shear layer has short life and sheds along with shear layer. As a consequence, the vortex in the first cavity becomes weaker and disintegrates. In addition, the reverse flow from the second cavity sometimes creates two to three small vortices in the first cavity as depicted in Fig. 6(e). Later, these small vortices merge into single vortex and are dampened out.

On the other hand, the vortices in the second and third cavities are well defined in the initial stage, with stronger vortex in the third cavity as compared to second cavity [Fig. 6(a)]. The directions of rotation of the vortices are counter-clockwise. As the shear layer separates out from girders, the fluid escapes out of second cavity and the vortex in the second cavity becomes weaker as seen from Figs. 6(b) ~ 6(c). With the movement of shear layer towards the girders, the vortex in the second cavity again strengthens [refer Figs. 6(d) ~ 6(f)]. However, it is important to mention that the vortex in the third cavity always remains stronger. It moves within the cavity from the right girder to left girder in the counter-clockwise direction. This vortex gets stronger when the shear layer comes closer and becomes weaker as the shear layer moves away, as a result of fluctuations. In addition to this a small vortex is also observed on the upstream side of first girder between shear layer and water surface that grows and diminishes in size continuously. The mean velocity represented in Fig. 6(g) illustrates the strong vortices within the second and third cavities.

Type II:

This is the flow type with higher Froude number as compared with flow Type I (F = 0.33 in this study). The shear layer emanating from the bottom edge of the upstream girder impinges directly near the third cavity. Initially, no vortices can be seen in any of the cavity as depicted in Fig. 7(a). With the time evolution, the vortices are generated in the second and third cavities. As the shear layer moves away from the bridge deck, the reverse flow occurs from the second cavity to the first one. As a result, a small vortex borns near the shear layer below the first cavity [Fig. 7(b)]. However, this vortex has very short life and it moves away with shear layer [refer Fig. 7(c)]. This process of formation of vortex at the bottom of cavity and its washing out is found to be a continuous phenomenon.

Moreover, in the second cavity, whenever the shear layer comes closer to the deck, a distinct counter-clockwise vortex is formed within the cavity and it revolves within the cavity as seen from Figs. 7(b) ~ 7(c). Conversely, when the shear layer goes away from the bridge deck, the vortex deteriorates due to outflow of the fluid from the cavity [Fig. 7(d)]. This process

https://doi.org/10.1017/jmech.2012.20 Published online by Cambridge University Press

continues with the progress of time. However, the vortex in the third cavity invariably remains strong and moves vertically inside the cavity. It comes down and becomes weak when the shear layer is separated, while it moves up with more strength as the shear layer comes closer [see Figs. 7(a) ~ 7(f)]. Further, small vortices also are observed on the upstream side of the first girder, which move downstream with the separation of shear layer. Sometimes, reverse flow is also detected from first cavity towards the upstream side of the first girder. The mean velocity field presented in Fig. 7(g) shows the separated shear layer and the strong vortices within the second and third cavities similar to flow Type I.

3.3 Mean Velocity Field in Shear Layer Below Bridge Deck

The instantaneous velocities measured by the PIV are ensemble averaged to obtain the mean velocity field below the bridge deck. Figure 8 shows the profiles of mean streamwise velocity u below the bridge deck non-dimensionalised by the mean approaching flow velocity u_0 at different non-dimensional streamwise distances x/H_1 for the flow Type I having $P_r = 2.00$ and $F = 0.20$. The logarithmic velocity profile of the approaching flow is influenced near the free surface by the presence of bridge deck as observed by the velocity profiles at non-dimensional streamwise distances $x/H_1 = -0.78$ and -0.56 where there exits a small reverse flow near the free surface. It indicates the formation of shear layer just on the upstream side of the girder. When the flow passes the upstream bridge girder the shear layer forms, which is evidenced by an apparent steep velocity gradient at $x/H_1 = 0.11$. Towards the downstream side with $x/H_1 > 0.11$, the thickness of shear layer increases and correspondingly the velocity gradient decreases. This causes the momentum transfer between the shear layer and vortices in the second and third cavities. As a result the vortices are very strong in the second and third cavities as discussed in previous section. The dashed line in Fig. 8 ($x/H_1 = 0.23$ to 0.90) indicates the bottom surface of the bridge deck. After crossing the bridge deck ($x/H_1 > 1.11$), the thickness of shear layer further increases but the shear layer moves towards the free surface. This creates certain vortex flow near the free surface on the downstream side of the deck as observed by the negative values of u/u_0 at sections $1.11 \leq x/H_1 < 1.90$. On the other hand, the mean streamwise velocity distribution below the shear layer is similar to that in the jet flow. However, near the bottom, the boundary layer flow predominates. This flow field can also be confirmed by the mean vector field depicted in Fig. 6(g). It is important to mention that velocity measurements were not possible above the bottom of the bridge girder at $x/H_1 = 0.44$ and 0.67 due to the presence of the girder. Similar velocity distributions were also observed for the case of flow Type II with slightly lower position of the shear layer.

The profiles of mean vertical velocity v below the bridge deck non-dimensionalised by mean approaching flow velocity u_0 at corresponding streamwise distances as in Fig. 8 for the flow Type I having $P_r = 2.00$ and $F = 0.20$ are presented in Fig. 9. In the approaching sections ($x/H_1 = -0.78$ to 0.23), the vertical velocity component is negative, implying the downward concentration of flow due to the constriction formed by the bridge deck. Beyond $x/H_1 = 0.44$, the v component is positive below the center of the shear layer and negative above the center of the shear layer. This represents the formation of counter-clockwise vortices near the shear layer as also evidenced in flow visualization images. The vortices above the shear layer breed continuously up to non-dimensional streamwise distance $x/H_1 = 1.34$. However, on the downstream side these vortices exit near the free surface as seen not only by the profiles of non-dimensional mean vertical velocity but also by the velocity field as show in Fig. 6(g). On the other hand, the non-dimensional mean vertical velocity v/u_0 is negligible below $y/H_1 < 0.5$. In other cases of flow Type II, analogous distributions of mean vertical velocity were also evidenced.

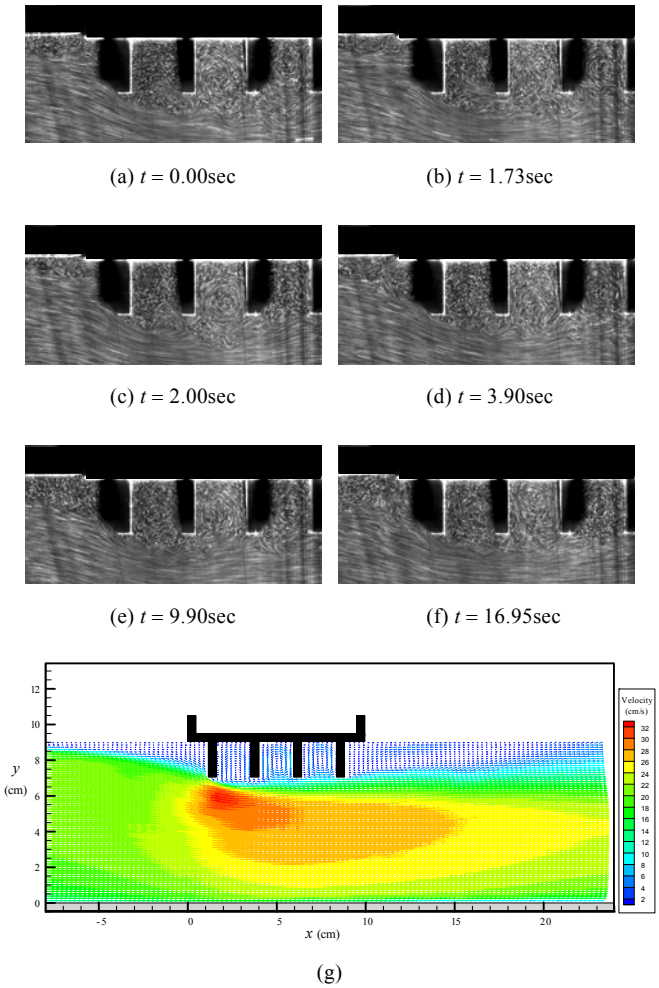
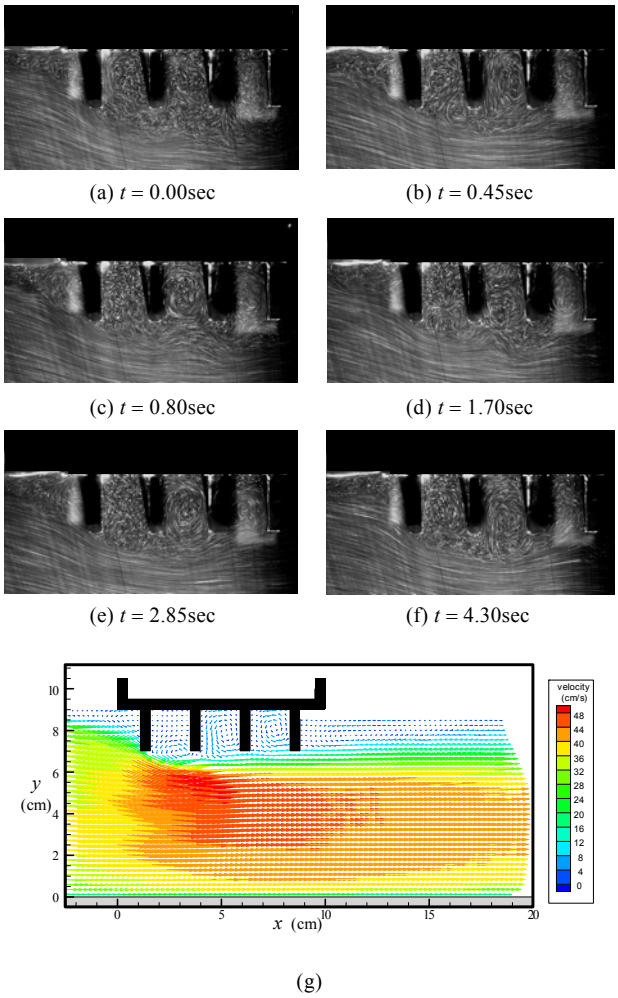


Fig. 6 (a)-(f) Images showing vortices in different cavities for flow Type I at time t = 0s, 1.73s, 2.0s, 3.9s, 9.9s, and 16.95s; (g) Mean velocity vector field for $P_r = 2.00$ and $F = 0.20$ (Case *B*)

https://doi.org/10.1017/jmech.2012.20 Published online by Cambridge University Press



(g)

Fig. 7 (a)-(f) Images showing vortices in different cavities for flow Type II at time t = 0s, 0.45s, 0.8s, 1.7s, 2.85s, and 4.3s; (g) Mean velocity vector field for P_r = 2.00 and F = 0.33 (Case *C*)

Further, the vertical distributions of non-dimensional mean streamwise velocity u/u_0 at certain non-dimensional streamwise distances x/H_1 within the boundary layer below the bridge deck for flow Type II with P_r = 2.00 and F = 0.33 (Case *C*) are illustrated in Fig. 10(a). From the variation it can be observed that, the vertical distributions of u/u_0 follow a standard boundary layer velocity profiles. However, $u/u_0 > 1$ as the flow is accelerated below the bridge deck. Using the regression equations fitted to the non- dimensional mean streamwise velocity profiles within the boundary layer, the boundary shear stress τ_b near the bottom is computed. The variation of boundary shear stress τ_b with non-dimensional streamwise distances x/H_1 for flow Type II with P_r = 2.00 and F = 0.33 (Case *C*) is presented in Fig. 10(b). Figure 10(b) illustrates the decreasing trend in the boundary shear stress with non-dimensional streamwise distances x/H_1.

3.4 Similarity Profile for Streamwise Velocity Within Shear Layer Below Bridge Deck

Furthermore, the similarity profile characterizing the non-dimensional mean streamwise velocity u/u_0 within the shear layer below the bridge deck is obtained following the analysis method proposed by Lin *et al*. [17] and thereafter adopted by Lin *et al*. [18]. The method of nonlinear curve fitting to the experimental data of non-dimensional mean streamwise velocity u/u_0 at different non-dimensional streamwise distances x/H_1 was adopted to determine the velocity and length scales for similarity profile of u/u_0 within the shear layer considering the flow cases of flow Type I and flow Type II. The non-dimensional mean streamwise velocity u/u_0 can be expressed by regression equation as:

$$\frac{u}{u_0} = -C_1 \tanh\left[C_2\left(\frac{y}{H_1}\right) + C_3\right] + C_4 \qquad (1)$$

where C_1 to C_4 are regression constants, which are given in Table 2 (for Type I - Case *B*) and Table 3 (Type II - Case *C*). Figure 11 demonstrates the satisfactory fitting of curves obtained by Eq. (1) to the experimental data of u/u_0 for flow Type I with P_r = 2.00 and F = 0.20, which implies that the velocity and length scales can be derived precisely from these curves.

Figure 12 shows different curves used for this purpose, for the flow Type I with P_r = 2.00 and F = 0.20 at non-dimensional streamwise distance x/H_1 = 1.67. The variation of non-dimensional mean streamwise velocity u/u_0, its first derivative $\partial(u/u_0)/\partial(y/H_1)$, and second derivative $\partial^2(u/u_0)/\partial(y/H_1)^2$ with respect to y/H_1 are plotted in Fig. 10. The first and second derivatives were calculated using u/u_0 fitting curves of Eq. (1). Note that the first derivative $\partial(u/u_0)/\partial(y/H_1)$ and the second derivative $\partial^2(u/u_0)/\partial(y/H_1)^2$ are very closely connected with the distributions of viscous shear stress and the slope of viscous shear stress, respectively. The position of center of the shear layer y_{sc}/H_1 is located where the value of $\partial(u/u_0)/\partial(y/H_1)$ is maximum as shown in Fig. 12. In addition, the representative upper bound y_{su}/H_1 and lower bound y_{sl}/H_1 of the shear layer were respectively defined at the points of extrema of $\partial^2(u/u_0)/\partial(y/H_1)^2$ [see Fig. 10]. The positions of upper bound y_{su}/H_1 and lower bound y_{sl}/H_1 do not indicate the points of zero shear stress, as the shear stress still exists beyond these extreme points as evidenced in Fig. 12. This facilitated in defining a specific velocity scale, $(u_{sl} - u_{su})$, where u_{su} and u_{sl} are the mean streamwise velocities at points y_{su} and y_{sl} respectively, and a specific length scale, $b_s = (y_{su} - y_{sl})$, to formulate the similarity velocity profile. Here, b_s denotes the representative thickness of the shear layer while $(u_{su} - u_{sl})$ represents the velocity deficit between the upper and lower bounds of the shear layer defined in b_s. Figure 13(a) shows the variation of center position of shear layer y_{sc}/H_1, upper bound y_{su}/H_1 and lower bound y_{sl}/H_1 of shear layer with the non-dimensional streamwise distance x/H_1. It is clear from Fig. 13(a) that the thickness of shear layer (that means specific length scale, b_s) increases with non-dimensional streamwise distance x/H_1. The variation of representative thickness b_s (normalized by approaching flow depth H_1) with non-dimensional streamwise distance x/H_1 presented in Fig. 13(b)

https://doi.org/10.1017/jmech.2012.20 Published online by Cambridge University Press

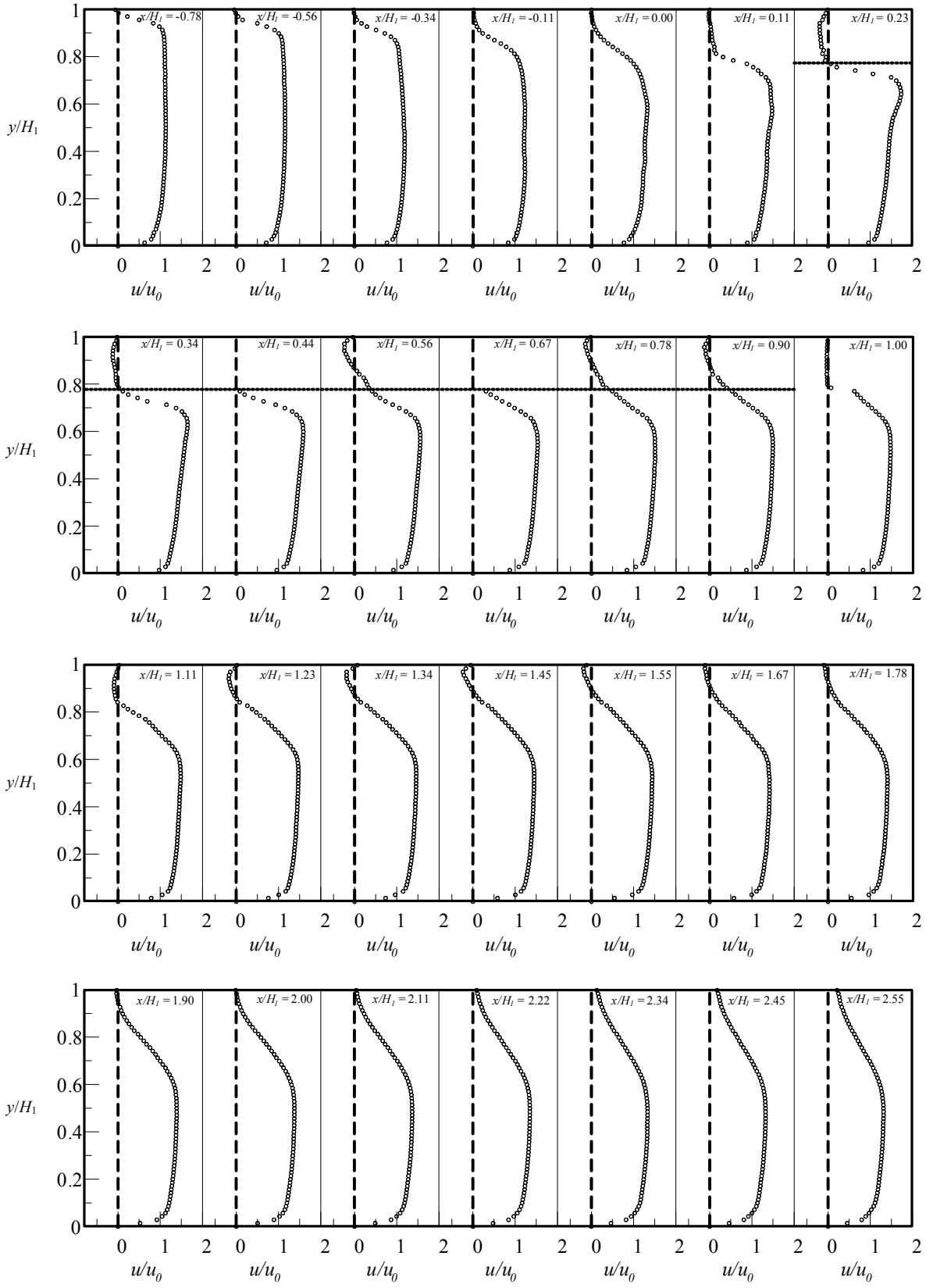


Fig. 8 Vertical distributions of non-dimensional mean streamwise velocity u/u_0 at different non-dimensional streamwise distances x/H_1 for flow Type I with $P_r = 2.00$ and $F = 0.20$ (Case *B*)

https://doi.org/10.1017/jmech.2012.20 Published online by Cambridge University Press

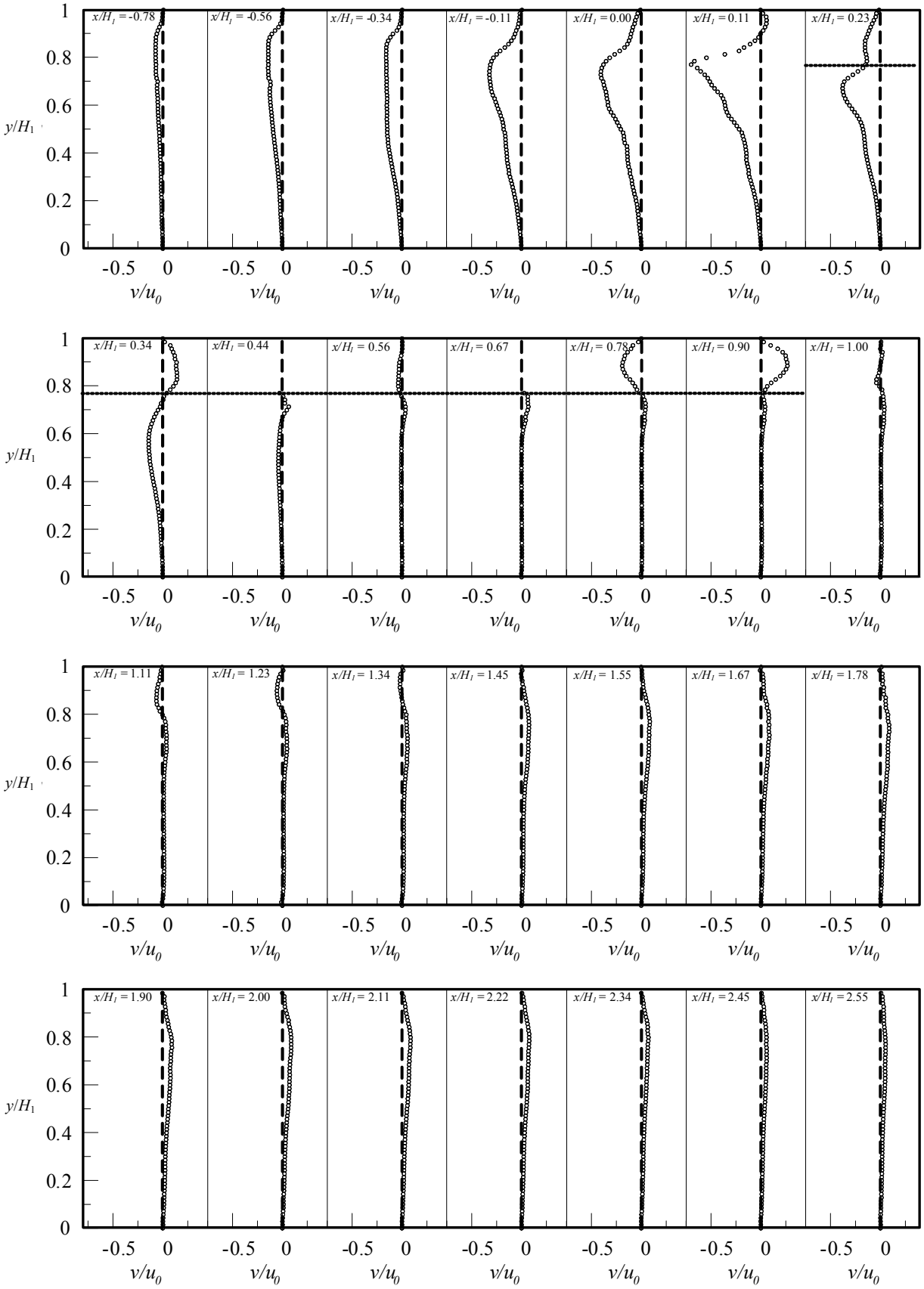


Fig. 9 Vertical distributions of non-dimensional mean vertical velocity v/u_0 at different non-dimensional stream-wise distances x/H_1 for flow Type I with $P_r = 2.00$ and $F = 0.20$ (Case *B*)

https://doi.org/10.1017/jmech.2012.20 Published online by Cambridge University Press

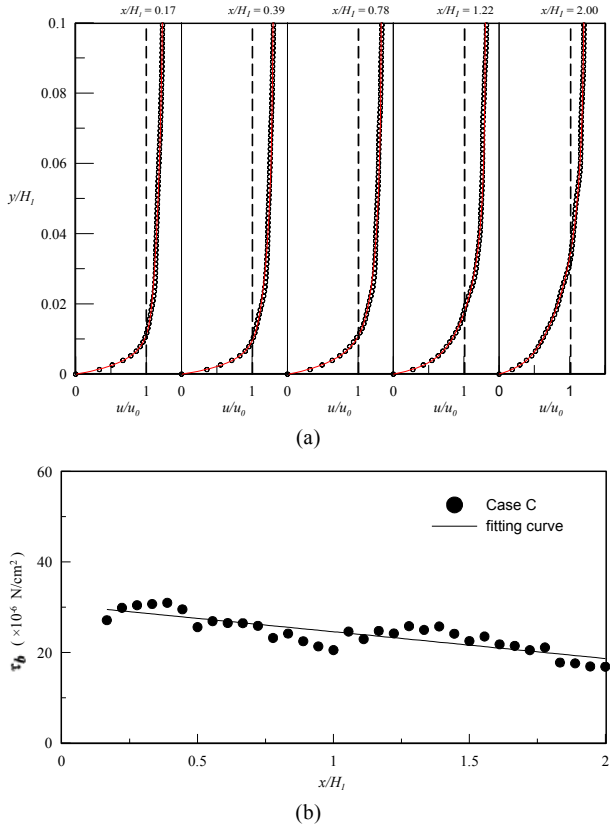


Fig. 10 (a) Vertical distributions of non-dimensional mean streamwise velocity u/u_0 at different non-dimensional streamwise distances x/H_1 within the boundary layer (red curve indicates the regression line), (b) Shear stress at bottom for flow Type II with P_r = 2.00 and F = 0.33 (Case *C*)

corroborates the increasing trend of non-dimensional representative thickness b_s / H_1 with non-dimensional streamwise distance x/H_1. It is interesting to observe that the increase in b_s / H_1 is very less under bridge deck portion for non-dimensional streamwise distance x/H_1 up to 1, while it is considerable for $x/H_1 > 1$. This is due to the suppression of shear layer below the bridge deck. Further, Fig. 13(c) represents the variation of specific velocity scale, $(u_{sl} - u_{su})$ normalized by mean approaching velocity u_0 with non-dimensional streamwise distance x/H_1. The value of $(u_{sl} - u_{su})/u_0$ is maximum at x/H_1 = 0.44 and it decreases continuously up to x/H_1 = 1 below the bridge deck portion. The specific velocity scale $(u_{sl} - u_{su})/u_0$ then increases for $1 < x/H_1 < 1.34$ and decreases further with x/H_1.

From the above analysis and discussion, $(u_{sl} - u_{su})$ and b_s are considered as the appropriate characteristic velocity and length scales for developing similarity profile. Accordingly, the variation of the dimensionless mean velocity deficit $(u - u_{su})/(u_{sl} - u_{su})$ versus the dimensionless shear layer thickness $(y - y_{sc})/b_s$ is plotted in Fig. 14 considering the experimental data of flow Type I not only with P_r = 1.00 and F = 0.24, but also with P_r = 2.00 and F = 0.13, 0.20, and flow Type II with P_r = 2.00 and F = 0.33. Further, in order to generalize the flow similarity model for different bridge deck conditions, the experiments were also carried out with bridge deck having three girders (Case *P* – Table 1) and no girder (rectangular block – Case *Q*, Table 1). Figs. 15 and 16 shown illustrate the mean velocity vector field for P_r = 2.00 and F = 0.20 for Case *P* and Case *Q* respectively. In these cases, the proximity ratio and Froude number were respectively P_r = 2.00 and F = 0.20. It is very much promising to observe the similar mean velocity vector field as in case of bridge deck with four girders [Fig. 6(g) having P_r = 2.00 and F = 0.20 (Case *B*) and Fig. 7(g) having P_r = 2.00 and F = 0.33 (Case *C*)]. Some of these data are also plotted in Fig. 14 to elucidate the applicability of the similarity model for most general case. It is interesting to observe collapse of all the experimental data onto a single band with a similarity profile being expressed by Eq. (2) having the R^2 value of 0.998 indicating that the proposed similarity profile can in general be used for obtaining mean streamwise velocity within the shear layer below the bridge deck.

$$\frac{(u-u_{su})}{(u_{sl}-u_{su})} = -0.866\tanh\left[1.314\left(\frac{y-y_{sc}}{b_s}\right)+0.002\right]+0.500 \quad (2)$$

The result shows a promising similarity profile corresponding to the shear layer below the bridge deck for flow Type I and flow Type II flow cases with different non-dimensional streamwise distances x/H_1. It should be noted that Eq. (2) follows the similar profiles as proposed by Lin *et al*. [17] for the shear layer in the sliding jet of a free overfall over a vertical drop (*i.e.*, without end sill) and Lin *et al*. [18] for the shear layer in the skimming flow over a vertical drop pool (*i.e.*, with an end sill).

3.5 Turbulence Characteristics

The turbulence characteristics such as vertical distributions of velocity fluctuations, in-plane turbulent kinetic energy and Reynolds shear stresses for flow Type I with P_r = 2.00 and F = 0.20 are presented in this section [Figs. 17(a) ~ 17(d)]. The velocity fluctuations in the streamwise and vertical directions are expressed in terms of rms values $U_{rms} = \sqrt{\overline{u'^2}}/u_0$ and $V_{rms} = \sqrt{\overline{v'^2}}/u_0$, where u' is the fluctuations in $u(t)$ and v' is the fluctuations in $v(t)$. Figure 13(a) presents the vertical distributions of U_{rms} along the non-dimensional streamwise distances x/H_1 = 0 ~ 2.55. The streamwise velocity fluctuations U_{rms} in the shear layer region are generally very high. In the approaching section (x/H_1 = 0 ~ 0.11), the magnitude of U_{rms} is 0.40 ~ 0.43, however, within the shear layer below the bridge deck (x/H_1 = 0.11 ~ 0.90) the value of U_{rms} becomes 0.74. This is the indication of high turbulence within the shear layer. Also, the peak value of U_{rms} within shear layer is found to occur near the center position, for the bridge deck portion (x/H_1 = 0.11 ~ 1.00). In addition, the distributions of U_{rms} in the streamwise directions show the asymmetry to the center position of the shear layer

https://doi.org/10.1017/jmech.2012.20 Published online by Cambridge University Press

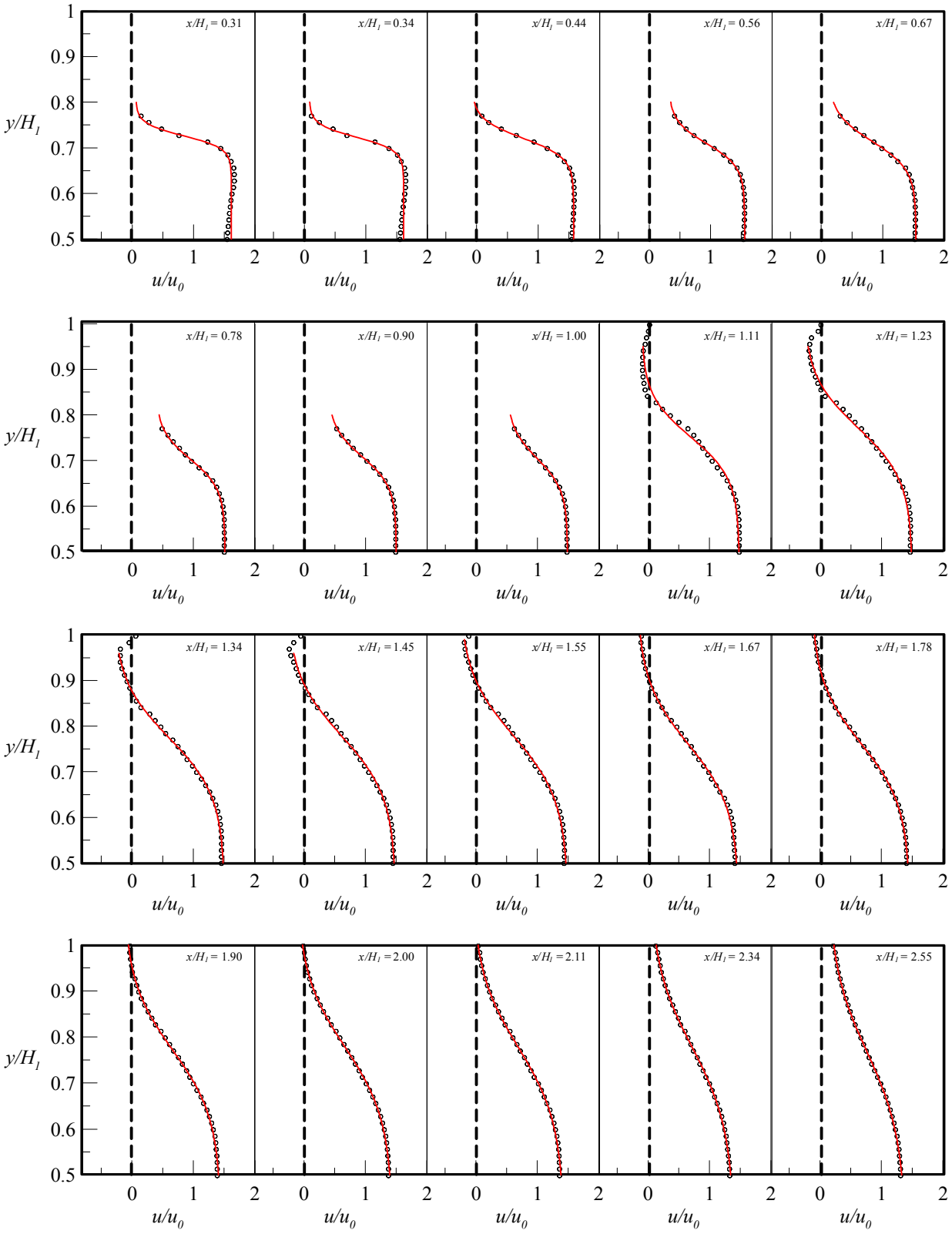


Fig. 11 Non-dimensional mean streamwise velocity u/u_0 profiles within shear layer at different non-dimensional streamwise distances x/H_1 with fitting curves for flow Type I with $P_r = 2.00$ and $F = 0.20$ (Case *B*)

https://doi.org/10.1017/jmech.2012.20 Published online by Cambridge University Press

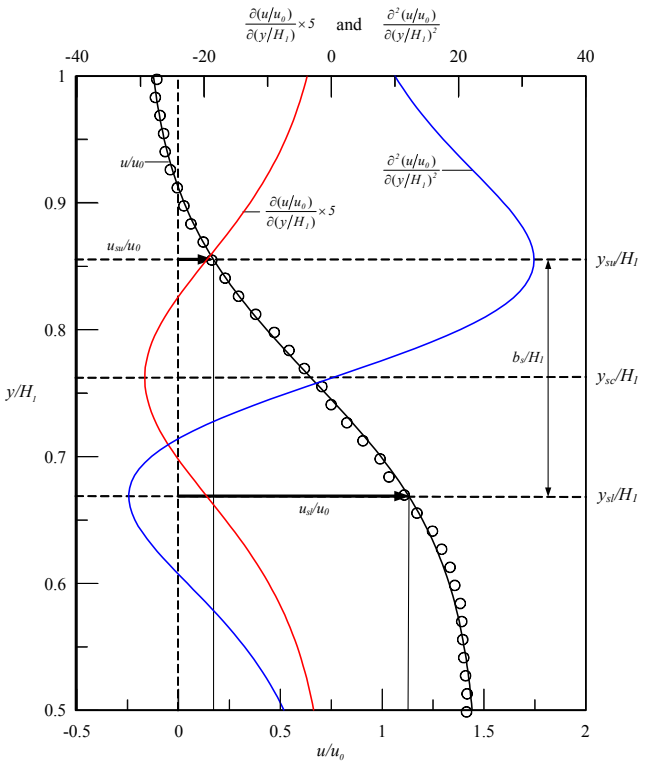


Fig. 12 Variation of u/u_0, $\partial(u/u_0)/\partial(y/H_1)$, and $\partial^2(u/u_0)/\partial(y/H_1)^2$ with y/H_1 at $x/H_1 = 1.67$ for flow Type I with $P_r = 2.00$ and $F = 0.20$ (Case *B*)

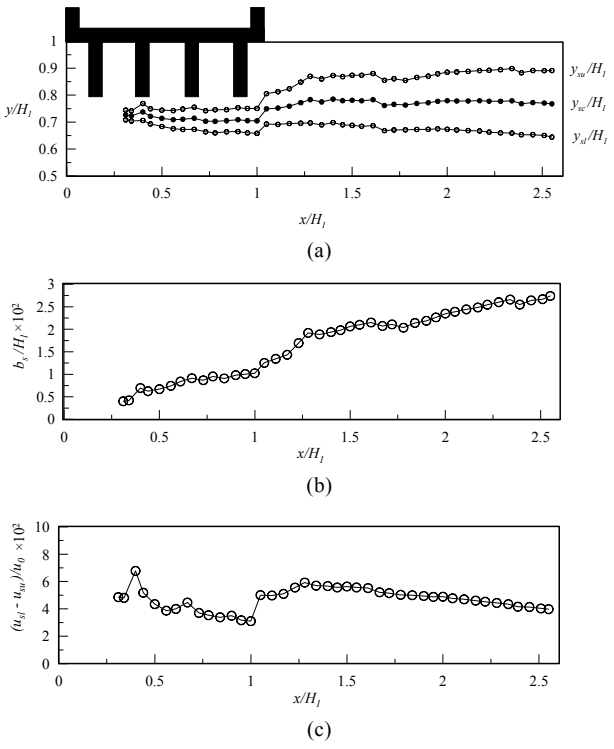


Fig. 13 (a) Variation of y_{sc}/H_1, y_{su}/H_1 and y_{sl}/H_1, (b) Variation of b_s/H_1, (c) Variation of $(u_{sl} - u_{su})/u_0$, with the non-dimensional streamwise distance x/H_1 for flow Type I with $P_r = 2.00$ and $F = 0.20$ (Case *B*)

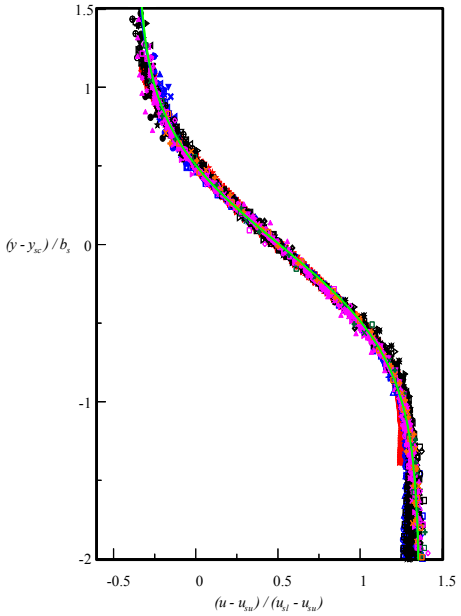
Table 2 Regression constants for Type I (Case *B*)

x/H_1	C_1	C_2	C_3	C_4	R^2
0.31	0.775	36.381	−26.432	0.835	0.996
0.34	0.767	34.640	−25.050	0.847	0.996
0.44	0.827	23.323	−16.828	0.748	0.999
0.56	0.617	19.663	−13.944	0.937	1.000
0.67	0.712	16.023	−11.446	0.827	0.999
0.78	0.564	15.345	−10.786	0.951	0.999
0.90	0.558	14.911	−10.573	0.944	0.999
1.00	0.495	14.274	−10.060	0.996	0.999
1.11	0.794	10.882	−8.185	0.691	0.993
1.23	0.887	8.640	−6.671	0.616	0.997
1.34	0.909	7.757	−6.012	0.601	0.999
1.45	0.888	7.388	−5.759	0.608	0.996
1.55	0.888	6.967	−5.428	0.611	0.998
1.67	0.831	7.058	−5.376	0.651	0.999
1.78	0.802	7.187	−5.485	0.662	1.000
1.90	0.789	6.682	−5.158	0.662	1.000
2.00	0.780	6.231	−4.856	0.663	1.000
2.11	0.750	5.989	−4.662	0.685	1.000
2.34	0.693	5.501	−4.285	0.714	1.000
2.45	0.660	5.538	−4.277	0.743	1.000
2.55	0.635	5.339	−4.100	0.763	1.000

Table 3 Regression constants for Type II (Case *C*)

x/H_1	C_1	C_2	C_3	C_4	R^2
0.21	0.774	28.773	−21.344	0.679	0.998
0.28	0.794	27.956	−20.385	0.721	0.998
0.34	0.797	26.660	−19.252	0.735	0.996
0.39	0.856	24.194	−17.375	0.688	0.998
0.45	0.795	26.172	−18.601	0.721	0.996
0.50	0.756	22.119	−15.661	0.759	0.999
0.56	0.736	17.332	−12.218	0.785	0.998
0.61	0.750	15.063	−10.643	0.775	0.998
0.67	0.764	15.130	−10.750	0.731	0.998
0.72	0.755	14.443	−10.265	0.728	0.999
0.78	0.731	13.649	−9.714	0.747	1.000
0.83	0.699	12.867	−9.149	0.782	0.998
0.89	0.741	11.614	−8.350	0.731	0.999
0.94	0.770	11.626	−8.411	0.685	0.991
1.00	0.788	10.038	−7.345	0.673	0.997
1.06	0.800	9.625	−7.108	0.658	0.997
1.11	0.839	8.469	−6.326	0.624	0.998
1.17	0.895	7.749	−5.878	0.578	0.999
1.22	0.903	7.614	−5.773	0.592	0.998
1.28	0.952	6.832	−5.274	0.538	0.998
1.33	0.901	7.197	−5.541	0.557	0.999
1.39	0.885	7.214	−5.541	0.575	0.999
1.44	0.872	7.254	−5.576	0.588	0.999
1.50	0.855	6.970	−5.371	0.591	0.999
1.56	0.827	7.122	−5.484	0.602	0.999
1.61	0.810	7.265	−5.559	0.608	0.999
1.67	0.788	6.958	−5.362	0.606	1.000
1.72	0.799	6.615	−5.105	0.623	0.999
1.78	0.769	6.867	−5.343	0.617	1.000
1.83	0.775	6.308	−4.927	0.612	0.999
1.89	0.753	6.215	−4.822	0.636	1.000

https://doi.org/10.1017/jmech.2012.20 Published online by Cambridge University Press



Type I						Type II	
$P_r = 1.00$ $F = 0.24$		$P_r = 2.00$ $F = 0.13$		$P_r = 2.00$ $F = 0.20$		$P_r = 2.00$ $F = 0.33$	
symbol	x/H_1	symbol	x/H_1	symbol	x/H_1	symbol	x/H_1
4 girder		4 girder		4 girder		4 girder	
	0.36		0.21		0.31		0.21
	0.73		0.28		0.34		0.28
	0.82		0.34		0.44		0.34
	0.91		0.39		0.56		0.39
	1.00		0.45		0.67		0.45
	1.09		0.50		0.78		0.50
	1.18		0.56		0.90		0.56
	1.27		0.61		1.00		0.61
	1.36		0.67		1.11		0.67
	1.45		0.72		1.23		0.72
	1.91		0.78		1.34		0.78
	2.00		0.83		1.45		0.83
	2.09		0.89		1.55		0.89
	2.18		0.94		1.67		0.94
	2.27		1.00		1.78		1.00
	2.36		1.06		1.90		1.06
	2.45		1.11		2.00		1.11
	2.55		1.17		2.11		1.17
	2.73		1.22		2.22		1.22
	2.82		1.28		2.34		1.28
	2.91		1.33		2.45		1.33
	3.00		1.39		2.55		1.39
	3.09		1.44	3 girder			1.44
			1.50		0.34		1.50
			1.56		0.66		1.56
			1.61		0.90		1.61
			1.67	rectangle			1.67
			1.72		0.33		1.72
			1.78		0.66		1.78
			1.83		0.90		1.83
			1.89				1.89
fitting curve							

Fig. 14 Similarity profile for mean streamwise velocity within shear layer below bridge deck for flow Type I and flow Type II cases

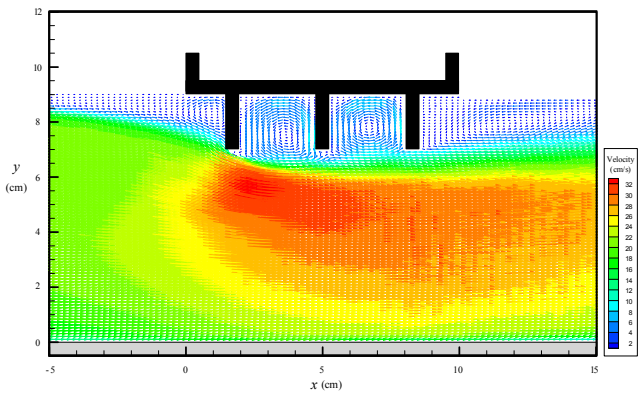


Fig. 15 Mean velocity vector field for P_r = 2.00 and F = 0.20 (Case P) with three girders

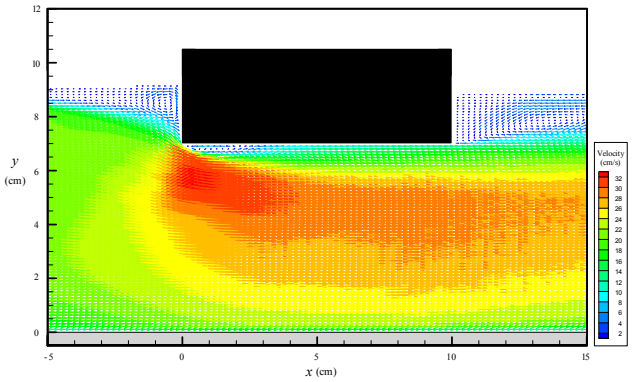


Fig. 16 Mean velocity vector field for P_r = 2.00 and F = 0.20 (Case Q) with rectangular block

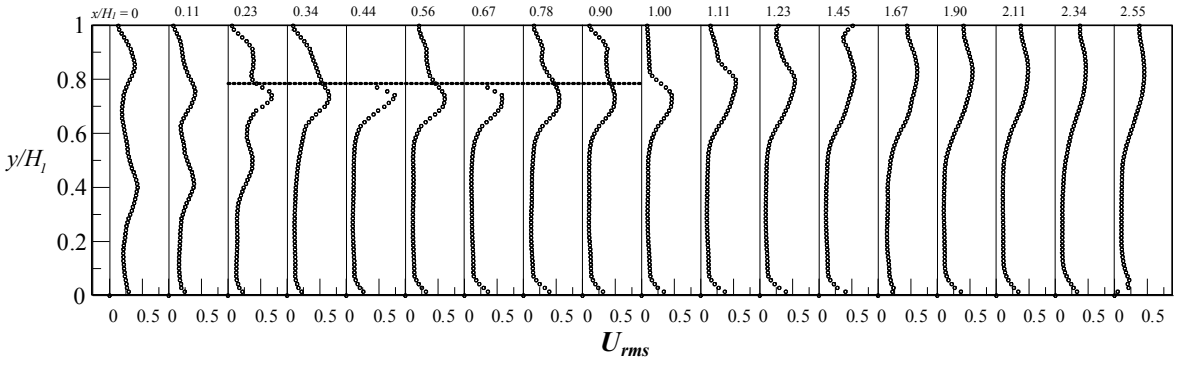
similar to the case of shear layer in skimming flow over vertical drop pool [18]. In the downstream direction, the value of U_{rms} within the shear layer reduces. On the other hand, below the shear layer, U_{rms} suddenly increases in the bottom boundary layer to a value of 0.32 ~ 0.42 and then decreases in the main flow portion in which U_{rms} almost remain constant at 0.1.

The distribution of vertical velocity fluctuations V_{rms} are shown in Fig. 17(b). In the approaching sections $x/H_1 = 0 - 0.11$, the distributions of V_{rms} are not well defined. Below the bridge deck, the distributions of V_{rms} within the shear layer follow the same trend as that of U_{rms}, however, their magnitude is 0.40 ~ 0.58. Also, the distributions of V_{rms} show the asymmetry to the center position of the shear layer similar to U_{rms}. The peak value of V_{rms} within shear layer is found to occur near the center position, for the bridge deck portion (x/H_1 = 0.11 ~ 1.00). On the downstream side of the bridge deck, within the shear layer the V_{rms} shows multimodal nature. In the bottom boundary layer, the slope of distribution of V_{rms} is very steep. Nevertheless, above the bottom boundary layer, the value of V_{rms} is nearly constant with value of 0.05 and then increases near the shear layer.

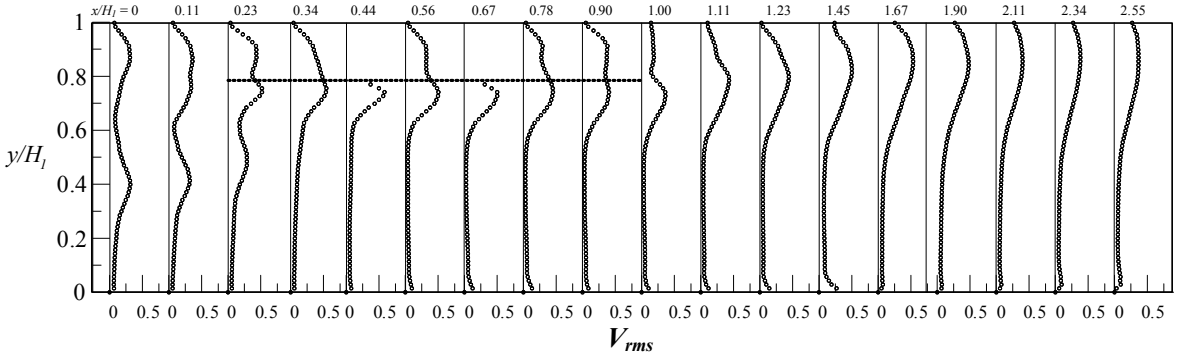
Figure 17(c) illustrate the vertical distributions of in-plane kinetic energy of turbulence in terms of $I = \sqrt{\overline{u'^2} + \overline{v'^2}} / u_0$. The profiles of in-plane kinetic energy of turbulence I are similar to that of U_{rms} profiles. In the approaching section, their magnitude is 0.18 ~ 0.53, except in the shear layer portion where its value is slightly higher. In the shear layer below bridge deck, the values of I reach peak value of 0.94 near the center of shear layer. However, the peak value decreases on the downstream side of the bridge deck. In the bottom boundary layer portion, I increases rapidly to a value of 0.42 and then decreases in the main flow portion.

The distributions of non-dimensionalized Reynolds stresses $\Lambda = -\overline{u'v'} / u_0^2$ relative to fluid density ρ, at different non-dimensional streamwise distances x/H_1 are presented in Fig. 17(d). The values of non- dimensional Reynolds stresses Λ are negligibly small in the entire main flow portion except in the shear layer

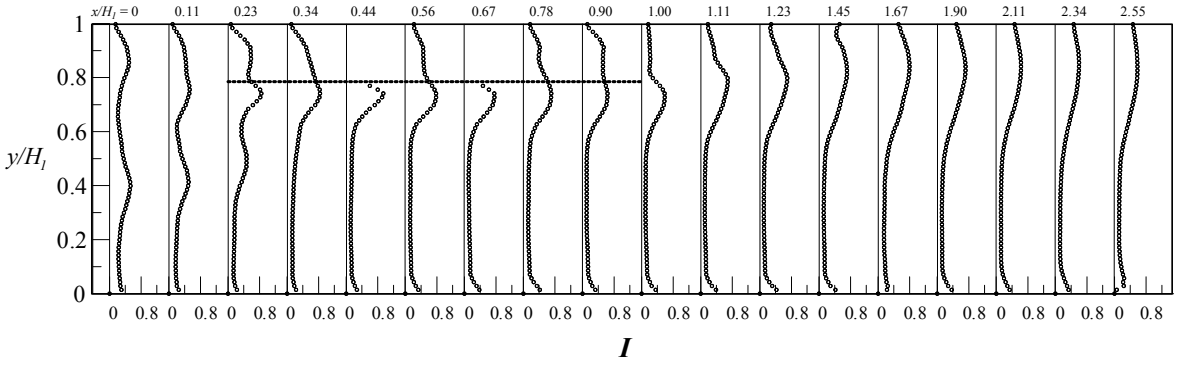
https://doi.org/10.1017/jmech.2012.20 Published online by Cambridge University Press



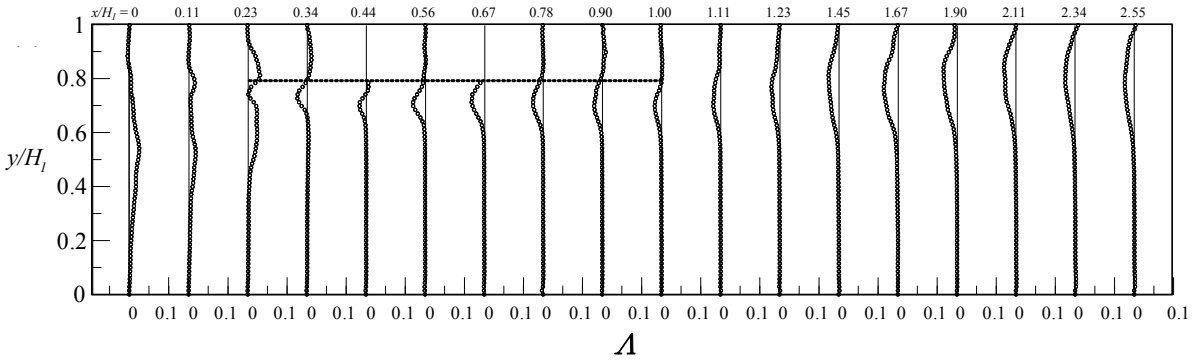
(a) U_{rms}



(b) V_{rms}



(c) In-plane kinetic energy of turbulence



(d) Non-dimensional Reynolds stresses Λ relative to fluid density

Fig. 17 Variation of turbulence characteristics below bridge deck for flow Type I with P_r = 2.00 and F = 0.20 (Case *B*)

https://doi.org/10.1017/jmech.2012.20 Published online by Cambridge University Press

where the values of Λ are negative. In the shear layer, the non-dimensional Reynolds stresses Λ have the maximum value of about −0.03 near the center position of the shear layer. In addition, the distributions of Λ within the shear layer show the symmetry about the center position of the shear layer. Based on the quadrant analysis [19], it was observed that the contributions of $u' - v'$ from quadrants I and III dominated over those from quadrants II and IV in the computation of non-dimensional Reynolds stresses Λ in the shear layer. For example, in flow Type I (Case *B*), with $P_r = 2.0$ and $F = 0.20$ at $x/H_1 = 0.34$ and $y/H_1 = 0.73$ ($H_1 = 9.0$cm), the contribution of $u' - v'$ in quadrant I was 35.3% and in quadrant III it was 18.9%, while in quadrant II it was 33.7% and in quadrant IV it was 12.1%. This would have resulted into the negative Reynolds stresses in shear layer. This point also refers to the location of maximum rms value of velocity fluctuations in the streamwise and vertical directions U_{rms} and V_{rms} as can be seen from Figs. 17(a) and 17(b). Interestingly, in-plane kinetic energy of turbulence I is also maximum at this point [refer Fig. 17(c)]. However, on the downstream side of the bridge deck, the distributions of non-dimensional Reynolds stresses Λ within the shear layer are not symmetric and also the maximum value of Λ decreases towards downstream direction. It is pertinent to mention that much similar turbulence characteristics are also observed for the case of flow Type II except near the free surface on the downstream side of bridge.

4. CONCLUSIONS

The experimental results of flow characteristics under a partially inundated bridge deck obtained by PIV and flow visualization technique are presented in the paper. The important findings are:

1. Based on Froude number of the approaching flow and proximity ratio studied, the flow structure under the bridge deck was categorized into four types. In flow Type I, the shear layer below the bridge deck being continuously fluctuating touches the soffit of all girders, and the water surface elevation on the downstream side of bridge deck is slightly lower than the counterpart on the upstream side. However, for the case of flow Type II, the shear layer impinges directly near the third cavity between the girders, while the water surface on downstream side of bridge deck is lower than the upstream one. However, in both the cases, the cavities between the girders are completely occupied by vortices, with stronger ones in the second and third cavities. On the other hand, the shear layer is separated from the bottom of upstream girder of the bridge deck in the cases of flow Type III and flow Type IV. In flow Type III, the flow impinges on the girders and cavities are partially filled with water; while the flow is totally separated from the deck bottom in flow Type IV case. Further, it is important to mention that, the flow downstream of the bridge deck is subcritical for all cases of flow Type I to flow Type IV.
2. The flow structures within the cavities between the bridge girders for flow Type I and flow Type II are discussed. It is observed that, the vortices in the second and third cavities are very strong as compared to the first cavity, in general. These vortices obtain energy from the shear layer. However, in the first cavity, there is large amount of fluctuations due to the turbulence of shear layer.
3. The profiles of mean streamwise and vertical velocity components are presented. The similarity profile for the mean streamwise velocity at different streamwise distances along the shear layer below the bridge deck was obtained using the measured streamwise velocities for flow Type I and II cases. The non-dimensionalised mean velocity deficit ($u_{sl} - u_{su}$) and non-dimensionalised specific length scale b_s (representative thickness) are considered as the appropriate characteristic velocity and length scales for developing similarity profile. The similarity profile proposed for mean streamwise velocity within shear layer is applicable to general cases of bridge deck having different numbers of girders even for a rectangular block without girders.
4. Further, the analysis method proposed by Lin *et al.* [17] for flow downstream of vertical drop (*i.e.*, free overfall) is more pertinent to obtain the similarity profile for the mean streamwise velocity of the shear layers beneath the bridge deck.
5. In addition, the vertical distributions of turbulence characteristics are also presented. All four all turbulence characteristics such as turbulent fluctuations U_{rms}, V_{rms}, in-plane kinetic energy of turbulence I and non-dimensionalized Reynolds stresses Λ have large magnitude in the shear layer. The distributions of U_{rms}, V_{rms} and I show the asymmetry to the center position of the shear layer, while the distributions of Λ show the symmetric variation about the center position of the shear layer. Further, the Reynolds stresses are negative in the shear layer and they are negligible in the main flow portion.

ACKNOWLEDGMENTS

The authors gratefully acknowledge the financial supports of this work by National Science Council (NSC), Taiwan, under Grant Nos. NSC 99-2221-E-005-117-MY3 and NSC 100-2119-M-005-001; and by Directorate General of Highway as well as National Freeway Bureau of the Ministry of Transportation and Communications (MOTC), Taiwan.

NOMENCLATURES

The following symbols are used in this paper:

B = overall width bridge deck [L];
b_s = representative thickness, specific length scale, ($y_{su} - y_{sl}$) [L];
C_i = regression constants, $i = 1 - 4$ [−];
D = total depth of deck [L];
F = approaching Froude number, $q/\sqrt{gH_1^3}$ [−];

https://doi.org/10.1017/jmech.2012.20 Published online by Cambridge University Press

F_B = Froude number calculated by Belanger equation [–];
g = gravitational acceleration $[LT^{-2}]$;
H_1 = approaching flow depth $[L]$;
h = clearance below bridge deck $[L]$;
I = in-plane kinetic energy of turbulence, $\sqrt{\overline{u'^2}+\overline{v'^2}}/u_0$ [–];
q = unit discharge, $u_0 \times H_1$ $[L^2T^{-1}]$;
R = Reynolds number, $\rho u_0 H_1/\mu$ [–];
t = time $[T]$;
U_{rms} = $\sqrt{\overline{u'^2}}/u_0$ [–];
u = mean streamwise velocity $[LT^{-1}]$;
u_0 = mean approaching velocity $[LT^{-1}]$;
u_{sl} = mean streamwise velocity at lower bound position of shear layer, y_{sl} $[LT^{-1}]$;
u_{su} = mean streamwise velocity at upper bound position of shear layer, y_{su} $[LT^{-1}]$;
u' = fluctuations in $u(t)$ $[LT^{-1}]$;
V_{rms} = $\sqrt{\overline{v'^2}}/u_1$ [–];
v = mean vertical velocity $[LT^{-1}]$;
v' = fluctuations in $v(t)$ $[LT^{-1}]$;
x = streamwise distance $[L]$;
y = distance normal to flume bed $[L]$;
y_1 = minimum flow depth below bridge deck $[L]$;
y_2 = flow depth at downstream of bridge deck $[L]$;
y_{sc} = center position of shear layer $[L]$;
y_{sl} = lower bound position of shear layer $[L]$;
y_{su} = upper bound position of shear layer $[L]$;
z = depth of girders $[L]$;
Λ = non-dimensionalized Reynolds stress relative to fluid density, $-\overline{u'v'}/u_0^2$ [–];
μ = dynamic viscosity $[ML^{-1}T^{-1}]$;
ρ = mass density $[ML^{-3}]$;

REFERENCES

1. Breusers, H. N. C., Nicollet, G. and Shen, H. W., "Local Scour Around Cylindrical Piers," *Journal of Hydraulic Research*, **15**, pp. 211–252 (1977).
2. Breusers, H. N. C. and Raudkivi, A. J., *Scouring, IAHR Hydraulic Structures Design Manual*, **2**, A. A. Balkema, Rotterdam, The Netherlands (1991).
3. Dey, S., "Local Scour at Piers, Part I: A Review of Development of Research," *International Journal for Sediment Research*, **12**, pp. 23–46 (1997).
4. Melville, B. W. and Coleman, S. E., *Bridge Scour, Water Resources Publications*, Fort Collins, Colorado (2000).
5. Richardson, E. V. and Davis, S. R., *Evaluating Scour at Bridges*, HEC18 FHWA NHI-001, Federal Highway Administration, US Department of Transportation, Washington, DC (2001).
6. Naudascher, E. and Medlarz, H. J., "Hydrodynamic Loading and Backwater Effect on Partially Submerged Bridges," *Journal of Hydraulic Research*, **21**, pp. 213–232 (1983).
7. Umbrell, E. R., Young, G. K., Stein, S. M. and Jones, J. S., "Clear-Water Contraction Scour Under Bridges in Pressure Flow," *Journal of Hydraulic Engineering*, **124**, pp. 236–240 (1998).
8. Jempson, M. A., "Flood and Debris Loads on Bridges," Ph.D. Thesis, Department of Civil Engineering, University of Queensland, St. Lucia (2000).
9. Picek, T., Havlik, A., Mattas, D. and Mares, K., "Hydraulic Calculation of Bridges at High Water Stages," *Journal of Hydraulic Research*, **45**, pp. 400–406 (2007).
10. Abed, L. M., "Local Scour Around Bridge Piers in Pressure Flow," Ph.D. Thesis, Department of Civil Engineering, Colorado State University, Fort Collins, Colorado (1991).
11. Arneson, L. A. and Abt, S. R., "Vertical Contraction Scour at Bridges with Water Flowing Under Pressure Conditions," *Transportation Research Record*, **1647**, pp. 10–17 (1999).
12. Verma, D. V. S., Setia, B. and Bhatia, U., "Constriction Scour in Pressurized Flow Condition," *International Journal of Engineering Transaction B: Applications*, **17**, pp. 237–246 (2004).
13. Lyn, D. A., "Pressure-Flow Scour: A Reexamination of the HEC-18 Equation," *Journal of Hydraulic Engineering*, **134**, pp. 1015–1020 (2008).
14. Junke, G., Kornel, K., Jorge, P. O. and Kevin, F., "Bridge Pressure Flow Scour at Clear Water Threshold Condition," *Transaction of Tianjin University*, **15**, pp. 79–94 (2009).
15. Malavasi, S. and Blois, G., "Influence of the Free Surface on the Flow Pattern Around a Rectangular Cylinder," *Proceedings of FLUCOME 2007— The Ninth International Symposium on Fluid Control, Measurement and Visualization*, September 16-19, Tallahassee, Florida (2007).
16. Lo, L. F., "Study on the Characteristics of Flow Field Under a Partially Inundated Bridge Deck," Master Thesis, National Chung Hsing University, Taiwan (2010).
17. Lin, C., Hwung, W. Y., Hsieh, S. C. and Chang, K. A., "Reply to the Discussion: Experimental Study on Mean Velocity Characteristics of Flow over Vertical Drop," *Journal of Hydraulic Research*, **46**, pp. 425–428 (2008).
18. Lin, W. J., Lin, C, Hsieh, S. C., Li, C. C. and Raikar, R. V., "Characteristics of Shear Layer Structure in Skimming Flow over a Vertical Drop Pool," *Journal of Engineering Mechanics*, **135**, pp. 1452–1466 (2009).
19. Soldati, A. and Monti, R., *Turbulence Structure and Modulation*, Springer-Verlag, New York (2001).

(Manuscript received December 22, 2010, accepted for publication June 28, 2011.)

https://doi.org/10.1017/jmech.2012.20 Published online by Cambridge University Press